Control Engineering Practice 178 (2027) 107262

Contents lists available at ScienceDirect

Control Engineering Practice

journal homepage: www.elsevier.com/locate/conengprac

Energy-based model predictive grid-forming control of the boost converter for dc grids ⋆

Marco Guerreiro *, Pedro dos Santos, Steven Liu

Chair of Control Systems, RPTU University Kaiserslautern-Landau, Gottlieb-Daimler-Straße, Kaiserslautern, 67663, Germany

A R T I C L E I N F O

Keywords:
DC microgrids
Grid-forming control
Grid-forming converters
Feedback linearization
Model predictive control

A B S T R A C T

Supercapacitors are a promising technology to handle power fluctuations in power systems. Fully leveraging their benefits, however, requires highly dynamic voltage control of their interfacing power converter. This paper presents a dynamic output voltage controller for a boost converter, a topology commonly used to interface supercapacitors with dc grids. The method is based on controlling the total energy of the converter as a means to shape its output voltage. Defining energy as the control variable allows the use of feedback linearization to transform the boost converter into an equivalent linear system. By mapping physical constraints of the converter to the resulting linear system, it is possible to use a predictive controller to control the total energy of the converter while meeting its physical constraints. The main advantage of the controller is that it is a single loop controller valid over the entire meaningful operating range of the converter. Moreover, by treating the converter in an energy-power domain, the controller is able to naturally handle constant power loads. The controller is verified in an experimental platform, where a boost converter is used to interface a supercapacitor bank with a constant power load.

1. Introduction

Microgrids are localized power systems that integrate local loads, generation, and storage, aiming for higher efficiency, resilience and sustainability in electricity supply (Lidula & Rajapakse, 2011; Liu et al., 2023). This local integration is one of the key features of microgrids, since it provides a way for the large-scale integration of distributed renewable energy sources, one of the main goals of the next-generation power system.

At a fundamental level, a microgrid or any power system in general is stabilized by balancing electricity generation and demand within the grid (Denholm et al., 2020; Lei et al., 2023). Mismatches in generation and demand are initially buffered by the elements of the grid that interface the sources and the loads and thus, the ability of the grid to handle sudden power imbalances depends on how much energy is available for buffering and how fast power can be transferred from the sources to the loads. The less energy available for buffering, the more stringent the dynamic power and control requirements on the sources become, and vice versa. The process of balancing generation and demand in a power system is denoted grid forming, and grid-forming units require two types of energy storage: buffering energy to initially compensate power imbalances, and bulk energy to supply loads in steady state.

In large scale systems based on synchronous generation, the buffering energy is primarily provided by the kinetic energy stored in the rotating masses of the generators, which is large enough to buffer power imbalances for seconds before the primary energy sources adjust their power output. In microgrids with high penetration of renewables, the buffering energy is primarily stored in the output capacitors of the power converters interfacing the sources and the grid, and it is considerably limited. With limited buffering energy, microgrids require grid-forming units with highly dynamic input sources, as well as converters with highly dynamic control loops to allow them to quickly transfer power from the sources to the loads. This becomes more critical in microgrids with high prevalence of constant power loads, which lead to more dynamic load changes in the system (Chang et al., 2020; Srinivasan & Kwasinski, 2020). In microgrids dominated by renewable energy sources, grid-forming units are usually powered by an energy storage system, with batteries being the most common type of technology (Mitali et al., 2022). However, grid-forming operation can have detrimental effects on the lifespan of batteries, because it requires repeated power cycles in short periods of time to handle power transients in the grid, and such continuous operation can negatively affect the health of batteries (Rocabert et al., 2019; Sharma et al., 2025; Zhang et al., 2024).

⋆ This work was supported by the Carl-Zeiss-Stiftung.

* Corresponding author.
E-mail address: marco.guerreiro@rptu.de (M. Guerreiro).

https://doi.org/10.1016/j.conengprac.2026.107262
Received 14 April 2026; Received in revised form 7 September 2026; Accepted 7 September 2026
Available online 11 September 2026

To ease the stress on battery systems, supercapacitors have been gaining increasing attention as an alternative to compensate power transients in the grid, while bulk energy storage systems handle steady-state loads (Engelbrecht et al., 2023; Iovine et al., 2019; Muralee Gopi et al., 2025). Supercapacitors are able to provide large current peaks in short periods of time, while charge and discharge cycles have no substantial effects on their lifespan. This makes them well suited for providing the short-term energy buffering required to reduce the dynamic power demands placed on bulk energy storage systems. To handle power transients while not supplying loads in steady state, supercapacitor-based grid-forming units have two controllers operating at different time scales. One controller slowly regulates the state-of-charge of the supercapacitor bank to ensure zero power transfer in steady state, while another controller provides grid-forming behavior in order to handle power transients. Thus, the ability of the supercapacitor-based unit to handle power transients is mostly determined by the dynamics of the grid-forming controller.

Grid-forming control of power converters is traditionally formulated as a voltage control problem, because the objective of the grid-forming converters is to stabilize the grid voltage while supplying the power demand of the loads (Hasan et al., 2025; Rosso et al., 2021). However, voltage control of some common step-up topologies is complicated by their constrained nonlinear and nonminimum phase dynamics. An alternative is to formulate grid forming as an energy regulation problem, since regulating the energy of the converter directly enforces the power balance between its input and output, and hence the grid-forming behavior. The main advantage of this formulation is that regulating the energy of some nonlinear nonminimum phase power converters is considerably simpler than directly controlling their output voltage (Guerreiro et al., 2024).

This article proposes an energy-based grid-forming controller for the boost converter. Feedback linearization is used to map the nonlinear nonminimum phase dynamics of the boost to an equivalent linear minimum phase system consisting of the converter's energy and power. The conditions under which the mapping is a diffeomorphism are evaluated to show that it is valid over the entire meaningful operating range of the converter. An optimal control problem is then formulated to stabilize the energy. To handle the physical duty cycle and current constraints of the converter, the constraints are mapped to the energy domain and included in the optimization. Since the resulting constrained optimal control problem is based on linear dynamics, its realization is considerably simplified.

Energy shaping of the boost converter has been explored before in different contexts, e.g. energy shaping in interconnection and damping assignment passivity-based control (IDA-PBC) (He & Ortega, 2020; Ortega et al., 2002; Pang et al., 2019), feedback linearization (Aouni & Dessaint, 2020; Xu et al., 2023; Zhang et al., 2023), and flatness-based control (Gensior et al., 2006; Gil-Antonio et al., 2019; Shahrouei et al., 2023). Compared to these methods, the method proposed in this paper mainly differs in two aspects. First, the energy representation of the boost converter is used in a meaningful way for grid-forming control. Energy *is* the system output, and it is actively shaped according to design requirements, which in turn directly shapes the output voltage response. This is in contrast with previous methods that use the energy only as a means to linearize the converter (Aouni & Dessaint, 2020; Xu et al., 2023; Zhang et al., 2023), or to ensure the closed-loop stability of a passive system output (He & Ortega, 2020; Ortega et al., 2002; Pang et al., 2019). Second, the method proposed in this paper explicitly handles the duty cycle and inductor current constraints of the converter. This is important for the safe operation of the converter and for the feedback linearization law that transforms the boost into its energy domain. The constraints are handled by a predictive controller that has a long prediction horizon but a straightforward implementation that is feasible for real-time operation, in contrast with previous approaches that used predictive control but did not consider constraints (Aouni & Dessaint, 2020; Gil-Antonio et al., 2019; Shahrouei et al., 2023; Zhang et al., 2023), used a short prediction horizon (Xu et al., 2023), or had more complicated implementation strategies (Gensior et al., 2006). The main advantages of the proposed controller are summarized as follows.

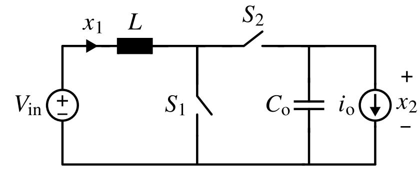

Fig. 1. Synchronous boost converter.

1. A single-loop grid-forming controller for the nonlinear nonminimum phase boost converter
2. The controller is valid over the entire meaningful operating range of the converter
3. Duty cycle and inductor current constraints are explicitly considered in the control design
4. Clear design procedure to obtain the parameters of the controller
5. The controller has a simplified real-time implementation consisting of forward computations only

The rest of this paper is organized as follows. Section 2 shows the energy formulation of the boost, and discusses the use of feedback linearization. Then, an optimal control problem is formulated for energy control, and the physical constraints of the converter are modeled in terms of the transformed boost system. Section 3 presents simulation and experimental results to show the feasibility of the proposed controller, comparing it to a conventional nonlinear cascaded approach and an advanced flatness-based control. Section 4 concludes this paper.

2. Constrained energy control of the boost converter

This section discusses the proposed controller. First, the model of the converter is presented, followed by a discussion on how the converter is transformed into a linear system in its energy domain through feedback linearization. Then, the predictive energy controller is presented, discussing the formulation of the problem and the transformation of the constraints. The last part of this section discusses voltage control and its design and implementation aspects.

2.1. Boost converter model

Fig. 1 shows the synchronous boost converter. The synchronous topology is considered here because its bidirectional power flow capability allows more dynamic energy changes in the converter. The input of the converter is represented by a voltage source V_{in} and the output is a constant power load, represented by a current source with current $i_{\text{o}} = P_{\text{o}}/x_2$, where P_{o} is the power of the load, and x_2 is the output voltage of the converter. The energy storage elements of the converter are the inductor L, with current x_1, and the output capacitor C_{o}. The converter is controlled through the active switches S_1 and S_2, operated in a complementary fashion.

For analysis and control, the average model of the converter is used, described by

$$L\dot{x}_1 = -x_2 + V_{\text{in}} + x_2 u \tag{1a}$$

$$C_{\text{o}}\dot{x}_2 = x_1 - i_{\text{o}} - x_1 u \tag{1b}$$

where u is the input signal of the average model, and is defined as the duty cycle of switch S_1.

2.2. Boost converter as an energy system

This section describes how the boost converter is represented as a linear system in terms of its energy and power. The main idea is to use the method of feedback linearization to find a suitable transformation that maps the current and voltage states of the boost to energy and power. The method of feedback linearization is not formally presented in this paper; see Isidori (1995) for a complete discussion.

The transformation starts by defining the system output y as the total energy of the converter, given by

$$y = \frac{1}{2}Lx_1^2 + \frac{1}{2}C_o x_2^2 \tag{2}$$

The goal is to find an expression that relates the derivative of the output y to the control input u. The first derivative of y can be found by inspection. If y is the total energy of the converter, the first derivative of y is the converter's power, which can be written as the difference between input and output power:

$$\dot{y} = V_{in}x_1 - P_o \tag{3}$$

where P_o is the power of the load. Since (3) does not contain the input signal u, its time derivative is taken. If V_{in} is assumed constant and if the load is a constant power load, then $\ddot{y}$ is

$$\ddot{y} = \frac{V_{in}}{L}\left(-(1-u)x_2 + V_{in}\right) \tag{4}$$

If u is chosen as

$$u = 1 - \frac{1}{x_2}\left(V_{in} - \frac{L}{V_{in}}v\right) \tag{5}$$

with $x_2 \neq 0$, expression (4) becomes

$$\ddot{y} = v \tag{6}$$

creating a linear relationship between the auxiliary input signal v and the total energy of the converter in the form of a double integrator system. For conciseness, the double integrator model (6) is written in terms of the state vector $z = \begin{bmatrix} z_1 & z_2 \end{bmatrix}^\intercal = \begin{bmatrix} y & \dot{y} \end{bmatrix}^\intercal$, resulting in

$$\begin{bmatrix} \dot{z}_1 \\ \dot{z}_2 \end{bmatrix} = \begin{bmatrix} 0 & 1 \\ 0 & 0 \end{bmatrix}\begin{bmatrix} z_1 \\ z_2 \end{bmatrix} + \begin{bmatrix} 0 \\ 1 \end{bmatrix}v \tag{7}$$

Now, the problem becomes that of controlling system (7), and stabilizing this system also stabilizes the original nonlinear system (1) (Isidori, 1995). This will be accomplished with a predictive controller, and will be discussed in Section 2.3.

Expressions (2) and (3) define the transform $T(x)$ that maps the voltage and current states (x) of the boost to energy terms (z), that is

$$z = T(x) = \begin{bmatrix} \frac{1}{2}Lx_1^2 + \frac{1}{2}C_o x_2^2 \\ V_{in}x_1 - P_o \end{bmatrix} \tag{8}$$

For feedback linearization, the transform $T(x)$ is only valid if it is a diffeomorphism on some domain $D \subset \mathbb{R}^2$, i.e. if the transform is bijective, continuously differentiable, and its inverse is continuously differentiable as well. The inverse transform of $T(x)$, $x = T^{-1}(z)$, can be found by writing the state vector x as a function of z, obtained by solving

$$x_1 = \frac{1}{V_{in}}z_2 + \frac{P_o}{V_{in}} \tag{9a}$$

$$x_2^2 = \frac{2}{C_o}z_1 - \frac{L}{C_o V_{in}^2}(z_2 + P_o)^2 \tag{9b}$$

for x. To completely solve for the inverse transform, it is necessary to take the square root of (9b). The square root is guaranteed to be real, since the right-hand side of (9b) is always greater than or equal to zero by definition. This ensures the existence of the inverse transform. Moreover, the transform $T(x)$ is bijective if x_2 is restricted to $x_2 > 0$. In practice, this is the case, since the steady-state output voltage of the boost is positive, and a startup strategy can be used to ensure that the output voltage is positive before the energy controller is enabled. Since transform (8) and its inverse (9) are continuously differentiable, transforming the nonlinear boost model (1) into the energy-power linear model (7) is valid for the entire meaningful operating range of the converter.

The main advantage of using energy as the output for feedback linearization is that the transformation induced by the feedback linearizing law (5) completely describes the dynamics of the boost. For grid-forming control, another option would be to directly choose the output voltage as the output for feedback linearization. However, in this case, the transformation resulting from the required linearizing law does not completely describe the dynamics of the boost, and there will be one internal state that is unobservable from the voltage state. In the case of the boost, the dynamics of this internal state is unstable (the nonminimum phase characteristic of the output voltage), and thus feedback linearization of the boost with voltage as the output is not feasible in practice.

Remark 1. In the boost converter, the duty cycle is strictly constrained to the interval $[0, 1]$. Consequently, the linearization induced by (5) remains valid only if the virtual signal v is selected such that the resulting duty cycle u stays within its physical limits. This condition is ensured by using a predictive controller that constrains the virtual signal v so as to satisfy the duty cycle constraints. This is discussed in Section 2.3.

Remark 2. Although the transformation (8) is nonlinear, it casts the original nonlinear nonminimum phase system (1) in the double integrator system (7), the major advantage of using the energy-based approach. The realization of the controller requires converting the physical voltage and current states of the converter to energy and power states using (8). This conversion only marginally increases the computational cost of the controller.

2.3. Constrained energy control

The transformation $T(x)$ given by (8) allows transforming the boost converter into the linear system (7), and now the control problem is that of controlling energy. By dynamically controlling energy, the grid-forming behavior is achieved and the output voltage will be shaped accordingly. However, the physical input of the converter, which is the duty cycle, is physically bounded to the $[0, 1]$ range. This means that the auxiliary signal v must be properly chosen so that the duty cycle remains within its bounds; otherwise, the linearization would no longer be valid. It is also important to limit the inductor current, in order to avoid damaging the inductor, the power semiconductors and the input source.

In order to have a dynamic control of energy while handling physical constraints imposed by duty cycle and inductor current, a model predictive controller is used. The formulation of the optimization problem is discussed next, followed by the formulation of the constraints.

2.3.1. Formulation of the optimization problem

The optimal control problem is formulated in a discrete-time setting, since the controller will be implemented in a digital platform. First, the linear system (7) is discretized and augmented with an integrator, leading to the model

$$z_a(k+1) = A_a z_a(k) + B_a \Delta v(k) \tag{10a}$$

$$y(k) = C_a z_a(k) \tag{10b}$$

where $\Delta v(k) = v(k) - v(k-1)$, $z_a(k) = \begin{bmatrix} \Delta z_1(k) & \Delta z_2(k) & z_1(k) \end{bmatrix}^\intercal$, $\Delta z_i(k) = z_i(k) - z_i(k-1)$, $i = 1, 2$, and matrices A_a, B_a and C_a are defined as

$$A_a = \begin{bmatrix} A_d & 0_{2\times 1} \\ C_d A_d & 1 \end{bmatrix} \tag{11a}$$

$$B_a = \begin{bmatrix} B_d \\ C_d B_d \end{bmatrix} \tag{11b}$$

$$C_a = \begin{bmatrix} 0_{1\times 2} & 1 \end{bmatrix} \tag{11c}$$

where A_d, B_d, and C_d represent the discretized model of (7). The additional integrator is used to compensate for nonidealities of the real converter that are not accounted for in model (1), which causes the transformation induced by feedback linearization to be non-exact.

To formulate the optimization problem, a standard cost function consisting of the error between a reference signal y^* and the output y is used.

The cost term J is given by Wang (2009)

$$J = \sum_{i=k_i}^{k_i+N-1} \left(y^*(i+1) - y(i+1)\right)^2 + r_w\left(\Delta v(i)\right)^2 \tag{12}$$

where N is the prediction horizon, k_i is the sampling instant and r_w is a weighting factor. The weighting factor r_w is used to select the aggressiveness of the controller, where larger values of r_w penalize fast changes in the control signal. Assuming the reference is constant over the entire prediction horizon, and using a condensed formulation, the cost function (12) can be written as a standard quadratic programming problem

$$\begin{aligned} \min_{\Delta V} \quad & J = \frac{1}{2}\Delta V^{\intercal} H \Delta V + \Delta V^{\intercal} E \\ \text{s.t.} \quad & M\Delta V \leq Q \end{aligned} \tag{13}$$

with $\Delta V = \left[\Delta v(k_i) \quad \cdots \quad \Delta v(k_i+N-1)\right]^{\intercal}$, $H = \Phi^{\intercal}\Phi + R_w$, $E = -\Phi^{\intercal}\left(1_N y^* - F z_{\mathrm{a}}(k_i)\right)$, and the matrix M and the vector Q represent the inequality constraints. The matrix R_w is given by $R_w = r_w I_N$. The matrices Φ and F result from the model and are defined as in Wang (2009).

2.3.2. Formulation of the constraints

Solving the optimization problem (13) results in the auxiliary signal v, which is then used to produce the corresponding duty cycle through the input transformation (5). Bounds on the auxiliary signal can be found by writing it as a function of the duty cycle:

$$v = \frac{V_{\mathrm{in}}}{L}\left(V_{\mathrm{in}} - (1-u)x_2\right) \tag{14}$$

Thus, the bounds $[v_{\min}, v_{\max}]$ for v can be found from the bounds $[u_{\min}, u_{\max}]$ on u. In a conventional formulation, the constraints on the input signal are enforced at every step of the prediction horizon. However, due to the nonlinear relationship between v and x_2, the bounds for $[v_{\min}, v_{\max}]$ in the prediction horizon become nonlinear, considerably complicating the solution of the optimization problem (13).

One way to handle this issue is to impose the constraints only on the first step of the prediction horizon. In this case, the constraints on v can be obtained based on the current measurement of x_2. Thus, assuming $u \in [0, 1]$, the bounds on the auxiliary signal v at instant k_i can be formulated as

$$v_{\min} = \frac{V_{\mathrm{in}}}{L}\left(V_{\mathrm{in}} - x_2(k_i)\right) \tag{15a}$$

$$v_{\max} = \frac{V_{\mathrm{in}}^2}{L} \tag{15b}$$

$$v_{\min} \leq v(k_i) \leq v_{\max} \tag{15c}$$

In practice, tighter bounds on the duty cycle may be chosen to avoid narrow gate pulses and other nonlinearities of the real converter, but this is not considered in this paper.

Another important set of constraints is that on the inductor current. These constraints can be written in terms of the converter's power, described by (3). Assuming that the power of the load can be measured, and that the inductor current is bounded by $[I_{\min}, I_{\max}]$, the bounds on the power of the converter are given by

$$V_{\mathrm{in}} I_{\min} - P_{\mathrm{o}} \leq z_2 \leq V_{\mathrm{in}} I_{\max} - P_{\mathrm{o}} \tag{16}$$

Although in this case the constraints are linear and could be imposed on the entire prediction horizon, they are only enforced on the first step as well, which helps reduce the size of the optimization problem that needs to be solved online. Thus, the constraints on z_2 at instant $k_i + 1$ are written as

$$z_{2,\min} = V_{\mathrm{in}} I_{\min} - P_{\mathrm{o}}(k_i+1) \tag{17a}$$

$$z_{2,\max} = V_{\mathrm{in}} I_{\max} - P_{\mathrm{o}}(k_i+1) \tag{17b}$$

$$z_{2,\min} \leq z_2(k_i+1) \leq z_{2,\max} \tag{17c}$$

assuming $P_{\mathrm{o}}(k_i+1) = P_{\mathrm{o}}(k_i)$ due to the constant power load.

The set of constraints (15) and (17) are written in terms of v and z_2; however, the optimization problem (13) is written in terms of ΔV, the sequence of optimal inputs to be determined. Thus, the constraints (15) and (17) need to be written in terms of ΔV. One possible formulation is

$$\begin{bmatrix} 1 & 0_{1\times(N-1)} \\ -1 & 0_{1\times(N-1)} \\ qB_{\mathrm{a}} & 0_{1\times(N-1)} \\ -qB_{\mathrm{a}} & 0_{1\times(N-1)} \end{bmatrix} \Delta V \leq \begin{bmatrix} v_{\max} - v(k_i-1) \\ -v_{\min} + v(k_i-1) \\ z_{2,\max} - z_2(k_i) - qA_{\mathrm{a}} z_{\mathrm{a}}(k_i) \\ -z_{2,\min} + z_2(k_i) + qA_{\mathrm{a}} z_{\mathrm{a}}(k_i) \end{bmatrix} \tag{18}$$

where $q = \begin{bmatrix} 0 & 1 & 0 \end{bmatrix}$. Physically, the set of constraints (18) imposes two upper bounds and two lower bounds of the first element of ΔV, making one of each redundant (the less restrictive one). Let $\Delta v_{\max}(k_i)$ and $\Delta v_{\min}(k_i)$ denote the minimum of the two upper bounds and the maximum of the two lower bounds, respectively. Then, the set of constraints (18) can be simplified to

$$\begin{bmatrix} 1 & 0_{1\times(N-1)} \\ -1 & 0_{1\times(N-1)} \end{bmatrix} \Delta V \leq \begin{bmatrix} \Delta v_{\max}(k_i) \\ -\Delta v_{\min}(k_i) \end{bmatrix} \tag{19}$$

This defines the inequality constraints of problem (13), where the left-hand side of (19) defines matrix M, and the right-hand side defines vector Q. Solving (13) then gives the control sequence ΔV for the entire prediction horizon N, while ensuring that the constraints (19) are met for the first step of the horizon, namely duty cycle and inductor current constraints. Following the receding horizon strategy, only the first element of the obtained sequence is used as an input to the actual system. Then, in the next sampling instant, the process is repeated.

In principle, it is possible that the set of constraints (19) becomes infeasible, i.e. the lower bound becomes greater than the upper bound. This infeasibility comes from the inductor current constraints, because the duty cycle constraints are always feasible (see (15)). Physically, this infeasibility means that a larger duty cycle than possible is required in order to satisfy the inductor current constraints. If infeasibility is detected, it can be handled by relaxing the inductor current constraints in order to make the set of constraints feasible. In practice, this infeasibility only happens if the duty cycle bounds are chosen to be a tight set around the nominal operating point, and there are large changes in the output load. In this article, the duty cycle is constrained in its full range, and no infeasibility issues have been detected in the simulation or experimental studies. Thus, the set of constraints (19) is assumed to always be feasible.

2.4. Output voltage control

A major objective in grid-supporting and grid-forming control is setting the output voltage of the converter. Since the proposed controller operates on the energy model of the converter, the desired voltage setpoint must be written in terms of energy. This is achieved by defining an energy reference

$$y^* = \frac{1}{2}L(x_1^*)^2 + \frac{1}{2}C_{\mathrm{o}}(x_2^*)^2 \tag{20}$$

where x_2^* is the output voltage reference, and $x_1^* = P_{\mathrm{o}}/V_{\mathrm{in}}$ is the reference for the inductor current.

Fig. 2 shows the block diagram of the proposed closed-loop system. Based on a voltage setpoint and measurements of the input voltage and load current, the energy setpoint y^* is obtained. The new setpoint and the converter's measurements are used to update the optimization problem (13), and solving it yields the auxiliary signal v that is then converted to a duty cycle and applied to the converter. The design of the controller and the details about the implementation of the online optimization required to realize the energy controller are discussed next.

2.4.1. Controller design

The proposed controller has two parameters that need to be selected, namely the prediction horizon N and the weighting factor r_w. These parameters are designed based on the procedure presented in

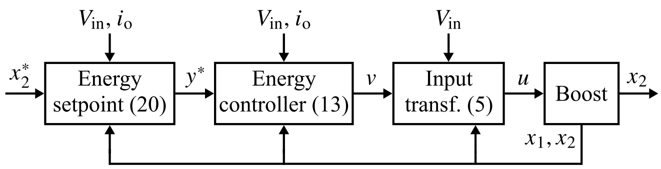

Fig. 2. Block diagram of the proposed control system.

Guerreiro et al. (2023), which obtains N and r_w based on a desired controller bandwidth. In summary, the method follows a two-step procedure. In a first step, a very long horizon is assumed and an r_w that meets the specified bandwidth is chosen. In a second step, the prediction horizon is adjusted to a sufficiently large value, such that the behavior of the system does not appreciably deviate from the case where the horizon is very long. For cases where most of the energy of the converter is stored in its output capacitor, designing the closed-loop response of the converter's energy will lead to a similar voltage response in terms of settling time and overshoot. The design method presented in Guerreiro et al. (2023) is based on the unconstrained system, so the designed bandwidth might not be met in practice when the controller enforces the constraints.

2.4.2. Controller implementation

Implementing the proposed controller requires solving the optimization problem (13) online, which can be challenging given the usual small sampling periods required to control the boost converter. However, because of how the constraints are formulated, and because of the receding horizon policy, the optimization problem has a very specific structure that can be leveraged to find the optimal control signal with forward computations only (Wang, 2009).

As discussed in Section 2.3.2, the physical constraints of the converter are enforced only on the first step of the prediction horizon, resulting in the constraints (19). These are constraints only on the first element of ΔV, that is, $\Delta v(k_i)$, which is the input to be applied following the receding horizon policy. Given this structure, the optimal $\Delta v^*(k_i)$ can be determined by finding the unconstrained solution to problem (13), retrieving $\Delta v^*_{\text{unc}}(k_i)$, and saturating it according to its bounds. Since problem (13) has an analytical solution for the unconstrained case, there is an analytical solution for $\Delta v^*_{\text{unc}}(k_i)$, and no online optimization is required to find the optimal $\Delta v^*(k_i)$.

The optimal Δv^*_{unc} at instant k_i can be written in the form of the state feedback law (Wang, 2009)

$$\Delta v^*_{\text{unc}}(k_i) = -K_e\left(y(k_i) - y^*(k_i)\right) - K_z \Delta z(k_i) \tag{21}$$

where $\Delta z(k_i) = \begin{bmatrix}\Delta z_1(k_i) & \Delta z_2(k_i)\end{bmatrix}^\intercal$, and $K_e \in \mathbb{R}$ and $K_z \in \mathbb{R}^{1\times 2}$ are given by

$$\begin{bmatrix}K_e & K_z\end{bmatrix} = \begin{bmatrix}1 & 0_{1\times(N-1)}\end{bmatrix}\left(\Phi^\intercal\Phi + R_w\right)^{-1}\Phi^\intercal F \tag{22}$$

The implementation of the energy controller depicted in the block diagram of Fig. 2 is represented in the block diagram of Fig. 3. At instant k, the states of the boost converter are transformed to energy and power, and are used to obtain the optimal unconstrained Δv with the state feedback law (21). The result is then saturated according to the bounds $\Delta v_{\min}$ and $\Delta v_{\max}$, which are given by (19).

As Fig. 3 shows, the implementation of the energy controller consists only of forward computations and is mostly static. The only parameters that need to be updated at every sampling instant are the bounds $\Delta v_{\min}$ and $\Delta v_{\max}$, but these are also forward computations. This results in a simple and yet effective controller that allows controlling the boost converter – a nonlinear system – in its entire operating range, while taking into account duty cycle and inductor current constraints.

Remark 3. The conventional way to study the closed-loop stability of predictive controllers is to choose the cost as a Lyapunov function, and then show that under recursive feasibility of the optimization the cost always decreases (Mayne et al., 2000). Since the cost function of the proposed predictive controller is formulated in terms of the total energy of the converter, it could be used as a Lyapunov function. However, the main complication is that recursive feasibility of the optimization cannot be ensured because the input and state constraints are enforced only on the first step of the prediction horizon. A stability analysis for such systems is a more general and theoretical problem that is outside of the scope of this paper.

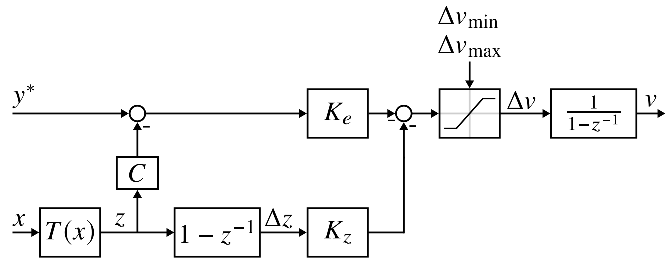

Fig. 3. Implementation of the online optimization.

3. Results

This section presents the results obtained with the proposed control strategy, denoted as Predictive Energy (PE) control. In the first part of this section, simulation results show a comparison between the PE controller and a conventional nonlinear cascaded controller. In the second part of this section, the proposed controller is validated in an experimental setup.

3.1. Simulation results

This section discusses simulation results obtained with the proposed controller, focusing on a comparison with a conventional nonlinear cascaded controller and an advanced flatness-based controller. For simulation, the ideal model (1) of the converter was used, with $L = 15$ μH, $C_o = 430$ μF, $V_{\text{in}} = 8$ V, nominal load of 80 W, and output voltage setpoint of 30 V. These are the same parameters used for the experimental validation.

For demonstration purposes, the proposed controller was designed to have a bandwidth of 2 kHz, using the procedure presented in Section 2.4. Based on this bandwidth, the sampling frequency of the controller was set to 25 kHz. Fig. 4 shows the results of the design procedure used to obtain the weighting factor r_w and prediction horizon N of the controller. First, the bandwidth of closed-loop system as a function of the weighting factor r_w is computed assuming a long horizon, as shown in Fig. 4a. This is based on the unconstrained system, which yields a static state feedback controller. For a bandwidth of 2 kHz, $r_w = 1.6 \cdot 10^{-4}$ is selected. With the selected r_w, the poles of the closed-loop system are plotted in the complex plane for different prediction horizons N, as shown in Fig. 4b. Decreasing the prediction horizon from 50 to 10 does not appreciably change the location of the poles, whereas decreasing it further starts moving the poles towards the outside of the unit circle, and a horizon of 3 or less results in an unstable controller. Thus, $N = 10$ is chosen as a sufficiently long horizon.

For comparison, two other controllers were also simulated. The controllers were designed to present the same 2 kHz bandwidth as the proposed controller. The first controller is a commonly used nonlinear cascaded controller where the inner loop uses feedback linearization to regulate the inductor current, and the outer loop is a proportional-integral controller that regulates the output voltage (Kim & Lee, 2015). The second controller is an advanced flatness-based controller, which uses energy as the flat output of the boost to precisely control the energy with an exponential trajectory, see e.g. Gensior et al. (2006), Shahrouei et al. (2023). Since these two controllers as implemented here do not account

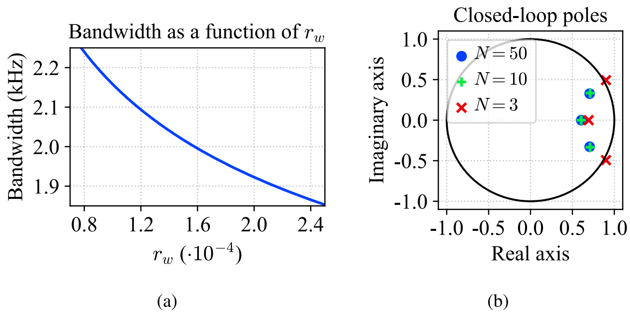

Fig. 4. Bandwidth of the unconstrained controller as a function of r_w for $N = 50$, and closed-loop poles as a function of N for $r_w = 1.6 \cdot 10^{-4}$.

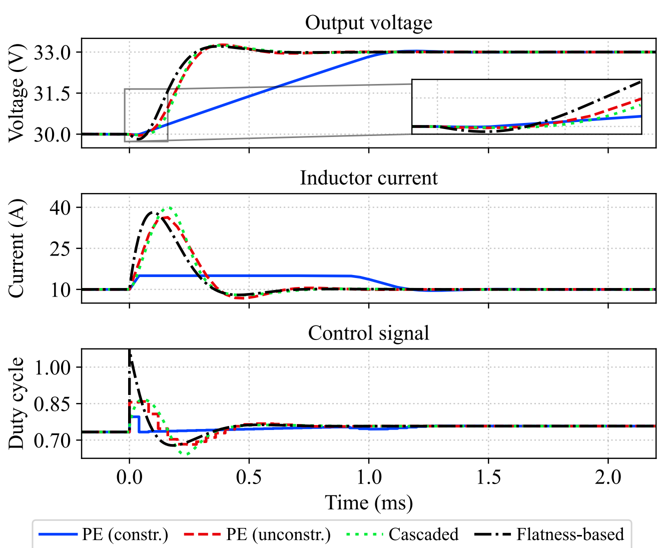

Fig. 5. Comparison of the output voltage transient for a 10% step of the nominal voltage at full load, for the proposed and cascaded controllers.

for constraints, a version of the proposed PE controller without constraints was additionally simulated for comparison purposes.

3.1.1. Voltage setpoint step

Fig. 5 shows the response of the closed-loop system with the PE, cascaded, and flatness-based controllers, when the voltage setpoint increases 10% from 30 V to 33 V at a constant power load of 80 W. As the figure shows, the response of the output voltage for the unconstrained PE, cascaded, and flatness-based controllers is similar. This result is expected since the controllers were designed to present a similar bandwidth. The main difference between these controllers is in the current and duty cycle waveforms. Compared to the cascaded controller, the responses of the unconstrained PE and flatness-based controllers are smoother and show a slightly lower current peak. However, the flatness-based controller violates the duty cycle constraints. Compared to the other controllers, the response of the constrained PE controller cannot meet the designed bandwidth and appears constrained to a limited operating region. This is because the controller is respecting the operating limits of the converter, which fundamentally limit the achievable bandwidth. It is worth mentioning here that the PE controllers are discrete in nature, while the cascaded and flatness-based controllers can be simulated entirely in continuous time.

3.1.2. Load step

Fig. 6 shows the response of the closed-loop system for a step change in the output load, from 30 W to 80 W at the nominal output voltage

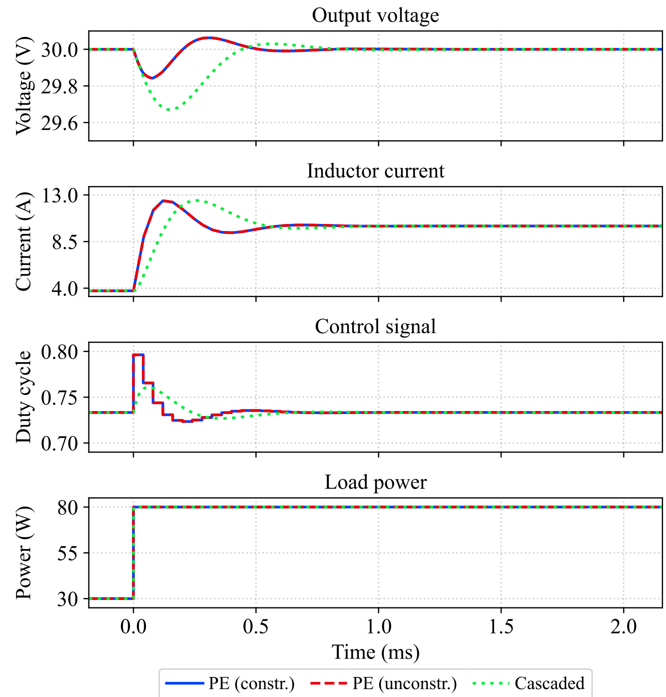

Fig. 6. Comparison of the output voltage transient for a 60% step of load at nominal voltage, for the proposed and cascaded controllers.

of 30 V. In this case, the response of the flatness-based controller is not simulated, as it requires an additional loop to handle disturbances. As the figure shows, the response of the constrained and unconstrained PE controllers is the same. This is because neither the duty cycle nor the inductor current reaches its respective limit, so the constrained PE controller operates as an unconstrained one. Moreover, compared to the cascaded controller, the PE controller shows smaller output voltage deviation and shorter settling time.

3.1.3. Robustness to parameter variation

Fig. 7 shows the closed loop response for parameter mismatches in the output capacitor C_o and inductor L. In each simulation, the values of the output capacitor C_o and the inductor L change with respect to their nominal values, C_n and L_n, but the controller is implemented assuming the nominal values only. Only two cases for parameter variation are shown, since they were verified in simulation to be the worst cases.

As Fig. 7 shows, the trajectory of the output voltage is only slightly affected by the variation in the assumed capacitance and inductance, and there is no steady-state error. This is due to the integral action embedded in the controller. Together, the incremental model (10) and the cost term (12) ensure zero steady-state error by providing a bias-free prediction model (by eliminating constant disturbances), and by accumulating on the input while the error is nonzero. A more noticeable effect of the parameter mismatch in the controller is the violation of the inductor current constraint. However, the violation is not that severe, and the controller is able to adjust the duty cycle such that the current is driven back within the constraints.

Remark 4. Variations in the input voltage are not studied because it is assumed that the input voltage can be measured. Measuring the input voltage is commonplace in larger converters for safe operation of the converter and its source. For example, when using a supercapacitor bank, it would be important to measure the input voltage in order to avoid overcharging the supercapacitor, or avoid operation with very low charge.

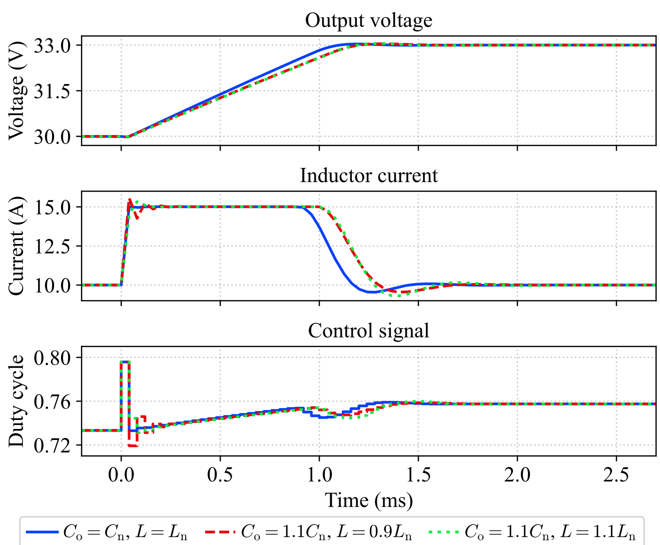

Fig. 7. Comparison of the output voltage transient for a 5% step of the nominal voltage at full load, for varying converter parameters L and C_o.

3.1.4. Discussion

Fig. 5 shows that the flatness-based controller is able to ensure a smooth response of the output voltage. Although there is a violation of the duty cycle constraint, this could be handled in different ways. One way would be to reduce the bandwidth of the controller, at the expense of performance. A better way would be to more carefully design the reference trajectory for the energy while accounting for duty cycle and inductor current constraints. However, designing this trajectory is not as straightforward as their inclusion in the PE controller. Moreover, the flatness-based controller is a feedforward linearizing strategy and cannot handle disturbances without an additional feedback loop, which requires additional design effort.

Fig. 6 shows that compared to a conventional nonlinear cascaded controller, the PE controller shows a better response to load changes. The reason is that the states of the proposed controller are the converter's energy and power (see (2) and (3)), which include information about the output load. This combined with the predictive behavior of the controller leads to a better response to changes in the load. And although the computational cost of the PE controller is higher than that of the cascaded controller, the overall computational load is still small and can be handled by modern digital signal processors.

While the cascaded controller implemented for comparison does not have feedback of the output load, this could be included in the design, which would improve its response. However, this further complicates the design and stability analysis of the closed-loop system, which is already approximated because the outer and inner loops are assumed to be decoupled. For the PE controller, the output load is naturally included in the model, and the stability of the closed-loop system is ensured for the unconstrained PE controller based on its design procedure (Guerreiro et al., 2023; Wang, 2009).

The results shown in Figs. 5 and 6 also highlight an important advantage of the PE controller. The voltage response of the closed-loop system is smooth despite the highly nonlinear region where the controller is operating. For large excursions around an already large duty cycle the behavior of the boost converter becomes highly nonlinear, yet the output voltage is smooth. The reason is that the PE controller operates in the energy domain, where it controls a linear system. By ensuring a smooth trajectory for the converter's energy, a smooth trajectory is ensured for the output voltage. Additionally, since the power of the converter is associated with the inductor current, a smooth power trajectory leads to a smooth current behavior.

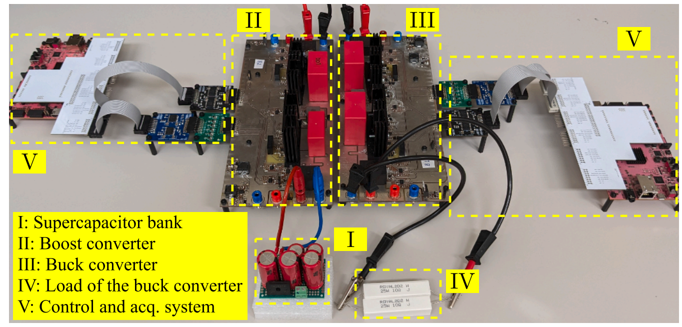

Fig. 8. Experimental setup.

Table 1
Parts used in the experimental setup.

Parameter	Value
V_{in}	6–9 V
L	15 µH (PULSE PA2248.153NLT)
C_o	430 µF (1x Nichicon UCS2C331MHD, 1x WIMA MKS 4 100 V)
MOSFETs	IRFB4127
Switching frequency	100 kHz
Inductor current sensor	ACS730KLCTR-20AB-T
Output current sensor	ACS712ELCTR-20A-T
Supercapacitor bank	12.5 F (3x WE 850617022002, 2x WE 850617022001)
ADCs	ADC121S021
Digital isolators	SI8641

An important advantage of using energy as a control objective is that it is physically meaningful and leads to a meaningful controller design. Because of the nonminimum phase characteristic of the output voltage, approaches such as feedback linearization and sliding mode control attempt to control the output voltage either indirectly through current, or by creating a virtual output that is a combination of current and voltage (AlZawaideh & Boiko, 2019; Arora et al., 2019). However, if this virtual output is not physically meaningful, it leads to a controller that is more difficult to interpret physically, design, and formulate the constraints.

3.2. Experimental validation

This section presents the experimental results obtained with the PE controller. The experimental setup and the details regarding the parameters of the controller are discussed next, followed by the experimental results of the closed-loop system for step changes in the voltage setpoint and in the output power.

3.2.1. Experimental setup

The experimental setup used to validate the controller is shown in Fig. 8, and consists of a supercapacitor bank, a boost converter, and a constant power load. The main parameters of the setup are shown in Table 1.

The supercapacitor bank has an equivalent capacitance of 12.5 F and rated voltage of 10.8 V. The bank is composed of a series connection of four 50 F capacitors, where one of them is a parallel connection of two 25 F capacitors. Before the experiment, the bank was charged to a voltage of around 9 V, and then used as input to the boost converter. Controlling the charge of the supercapacitor bank is not discussed in this paper. This would be achieved with an outer state-of-charge controller, which is out of the scope of this paper.

The synchronous boost converter is an experimental platform consisting of a printed-circuit board containing the power stage of the boost and additional circuitry for measurements and signaling. The input voltage of the boost converter comes from the supercapacitor bank, and its output is connected to the load. The load is a constant power load comprising a synchronous buck converter feeding a resistive load. Power steps are obtained by changing the voltage setpoint of the buck converter.

Both converters are controlled with Zynq-7000 System-on-a-Chip (SoC) platforms, consisting of a dual-core processor and a field-programmable gate array (FPGA) embedded on the same chip (Guerreiro et al., 2022). The control algorithms are executed in one of the cores of the processor, while the other core runs a command-line interface. The FPGA is used to interface with the converters by generating the gate signals for the MOSFETs and controlling the analog-to-digital converters (ADCs). The gate signals are generated based on a triangular carrier, and the ADCs are triggered when the carrier reaches its maximum value, so that the average value of the inductor current is sampled.

For the experimental validation, the proposed controller was designed to present a bandwidth of 1 kHz, chosen as a compromise between the controller's response and its susceptibility to measurement noise. Based on this bandwidth, a sampling frequency of 25 kHz was chosen, and the design procedure discussed in Section 2.4 resulted in $r_w = 0.01$ and $N = 30$. The bounds for the duty cycle were computed taking into account the delay introduced by the PWM of one switching cycle. Moreover, an exponential moving average filter was used in order to filter the output current measurement used in the control algorithm. The cut-off frequency of the filter was set to 8 kHz. Since this frequency is much higher than the bandwidth of the controller, the filter can be ignored during control design.

Remark 5. All waveforms shown in the results presented in this section were obtained with the SoC-based controllers. The waveforms show the raw measurements seen by the controller, without any filtering, digital or analog. The only processing that is applied to the raw measurements is the conversion from raw values to corresponding calibrated voltage and current values.

3.2.2. Voltage setpoint changes

Fig. 9 shows the response of the proposed controller to a 10% change in its voltage setpoint, from 30 V to 33 V, at full load. The PE controller is able to drive the output voltage to the new reference in about 4.5 ms, while keeping the inductor current at its predefined upper limit of 15 A. There is a small violation in the current constraint, but this is quickly compensated by the controller. In this case, the controller is not able to keep the designed bandwidth of 1 kHz, since this is not physically possible due to the constraints of the converter.

Fig. 10 shows the response of the PE controller for a 10% decrease in the output voltage, from 30 V to 27 V. Contrary to the step-up case, now the controller has much more headroom to drive the inductor current. For this reason, the output voltage is regulated to the new reference value much faster, with a settling time of around 2.4 ms. Combined with the undershoot of about 20.5%, the bandwidth of the controller is estimated at around 0.77 kHz.

As Figs. 9 and 10 show, the converter input voltage can vary considerably during transients. This is due to the relatively large parasitic resistance in the connection between the supercapacitor bank and the boost prototype. However, because the controller uses the input voltage measurement as feedback, it is able to adapt to these variations.

3.2.3. Load step

Fig. 11 shows the response of the controller to a step in the power of the load. Initially, the setpoint for the output voltage is set to 30 V, and the converter supplies approximately 40% of its full load. Then, the load steps up by about 60% of the full load with a rise time of around 0.5 ms. The voltage drop of the proposed controller is about 0.7 V, but is regulated back to within 99% of the setpoint within 0.8 ms, while satisfying the constraints on the inductor current.

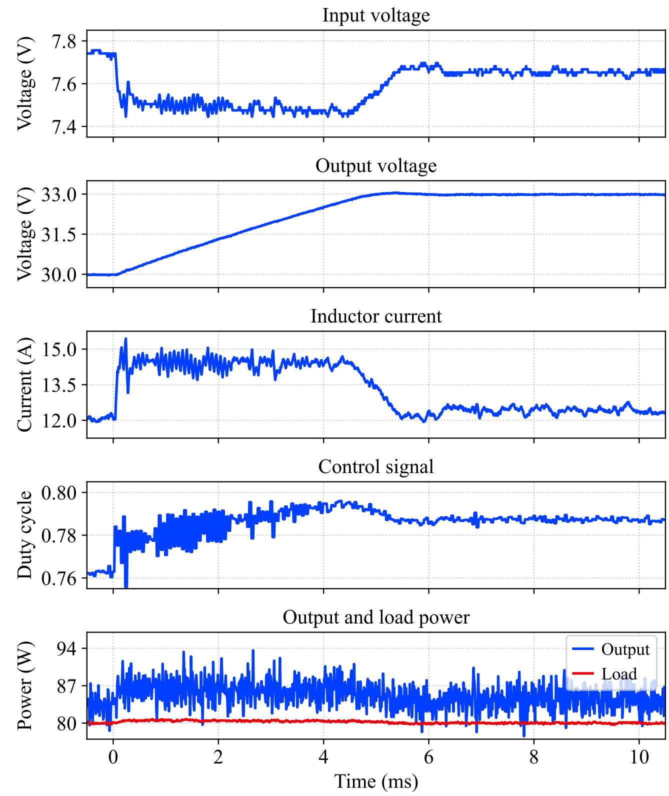

Fig. 9. Output voltage transient for a 10% step of the nominal voltage at full load.

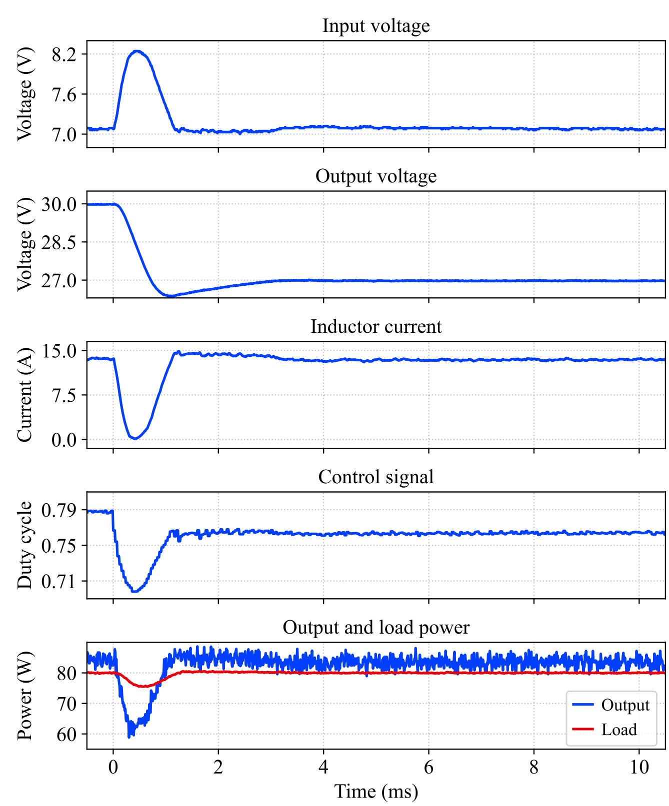

Fig. 10. Output voltage transient for a -10% step of the nominal voltage at full load.

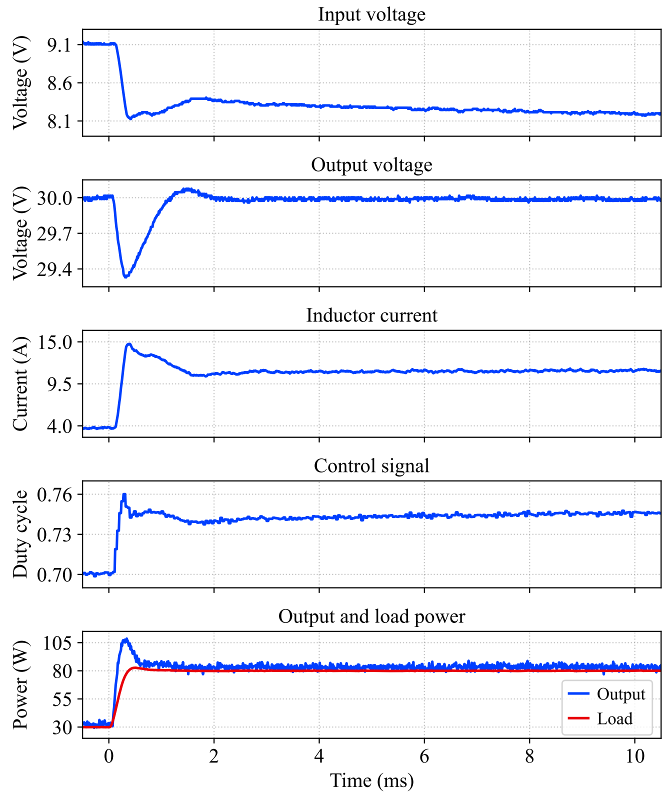

Fig. 11. Output voltage transient for a 60% step in output power at nominal voltage.

3.2.4. Discussion

The experimental results validate the operation of the proposed controller, which is able to stabilize the output voltage of the boost converter driving an active load, despite operating in a highly nonlinear region, with variations on the input voltage, and large excursions in the duty cycle. However, there are some differences between the experimental and simulation results.

In the simulation results shown in Figs. 5 and 7, the duty cycle is smooth during the constrained operation of the controller. However, in the experimental results shown in Fig. 9, the duty cycle appears much more noisy, which in turn affects the inductor current. The main reason for this behavior is noise in the estimation of the output power. As shown in Fig. 9, there can be fluctuations of several watts in the measurement of the output power. When the controller is constraining the inductor current, these fluctuations cause sudden changes in the saturation bounds of the duty cycle (see (17)), which in turn lead to sudden changes in the value of the duty cycle. This behavior can be reproduced in the ideal simulation study presented in Section 3.1 by introducing noise in the estimation of the output power. One way to improve this behavior is to filter the output current. In this case, either the bandwidth of the controller needs to be reduced, or the filter needs to be included in the model of the system, which would increase complexity.

Another main difference from the simulated model is the load. Although an ideal constant power load is used in the simulation, it is physically realized with another voltage-controlled converter, which has its own dynamics. This can be seen in the results shown in Fig. 10. Changing the output voltage of the boost causes a disturbance in the load, which rejects this disturbance according to the dynamics of its voltage controller.

4. Conclusion

Fully leveraging the advantages of supercapacitors in grid-supporting units requires converters with highly dynamic voltage control loops. This paper presented a dynamical constrained grid-forming controller for a boost converter. The proposed controller overcomes the challenging nonlinear and nonminimum phase characteristics of the boost converter by transforming it into an energy-power system. In the energy domain, the converter presents a linear behavior, and a model predictive controller based on a linear model can be used to achieve a dynamic response. The main advantages of the proposed controller include its inherent ability to handle constant power loads, and its operation in the entire meaningful range of the converter while accounting for physical constraints of the converter. Future development will be focused on improving feedback linearization to be robust to parameter variations, possibly as a way to replace the integrator in the predictive controller by accounting for model mismatches directly in the linearization law, and a formal stability proof of the proposed controller.

CRediT authorship contribution statement

Marco Guerreiro: Writing – review & editing, Writing – original draft, Visualization, Software, Methodology, Investigation, Formal analysis, Data curation, Conceptualization; **Pedro dos Santos:** Writing – review & editing, Resources, Methodology, Formal analysis, Conceptualization; **Steven Liu:** Writing – review & editing, Supervision, Software, Resources, Methodology, Funding acquisition, Formal analysis, Conceptualization.

Declaration of competing interest

The authors declare that they have no known competing financial interests or personal relationships that could have appeared to influence the work reported in this paper.

References

AlZawaideh, A., & Boiko, I. (2019). Analysis of a sliding mode boost converter under fluctuating input source voltage, using LPRS method. *Control Engineering Practice*, *92*, 104132. https://doi.org/10.1016/j.conengprac.2019.104132

Aouni, W. E., & Dessaint, L.-A. (2020). Real-time implementation of input-state linearization and model predictive control for robust voltage regulation of a DC-DC boost converter. *IEEE Access*, *8*, 192101–192108. https://doi.org/10.1109/ACCESS.2020.3032327

Arora, S., Balsara, P., & Bhatia, D. (2019). Input–output linearization of a boost converter with mixed load (Constant voltage load and constant power load). *IEEE Transactions on Power Electronics*, *34*(1), 815–825. https://doi.org/10.1109/TPEL.2018.2813324

Chang, F., Cui, X., Wang, M., Su, W., & Huang, A. Q. (2020). Large-signal stability criteria in DC power grids with distributed-controlled converters and constant power loads. *IEEE Transactions on Smart Grid*, *11*(6), 5273–5287. https://doi.org/10.1109/TSG.2020.2998041

Denholm, P., Mai, T., Kenyon, R. W., Kroposki, B., & O'Malley, M. (2020). Inertia and the power grid: A guide without the spin. https://www.nrel.gov/docs/fy20osti/73856.pdf.

Engelbrecht, T., Isaacs, A., Kynev, S., Matevosyan, J., Niemann, B., Owens, A. J., & Grondona, B. S. A. (2023). STATCOM technology evolution for tomorrow's grid: E-STATCOM, STATCOM with supercapacitor-based active power capability. *IEEE Power and Energy Magazine*, *21*(2), 30–39. https://doi.org/10.1109/MPE.2022.3230969

Gensior, A., Woywode, O., Rudolph, J., & Guldner, H. (2006). On differential flatness, trajectory planning, observers, and stabilization for DC–DC converters. *IEEE Transactions on Circuits and Systems I: Regular Papers*, *53*(9), 2000–2010. https://doi.org/10.1109/TCSI.2006.880342

Gil-Antonio, L., Saldivar, B., Portillo-Rodríguez, O., Vázquez-Guzmán, G., & De Oca-Armeaga, S. M. (2019). Trajectory tracking control for a boost converter based on the differential flatness property. *IEEE Access*, *7*, 63437–63446. https://doi.org/10.1109/ACCESS.2019.2916472

Guerreiro, M., dos Santos, P., & Liu, S. (2023). On the design of a model predictive controller for a DC-DC buck converter. In *25th European conference on power electronics and applications* (pp. 1–8). https://doi.org/10.23919/EPE23ECCEEurope58414.2023.10264352

Guerreiro, M., dos Santos, P., & Liu, S. (2024). Voltage control of the Ćuk converter for grid-forming in DC grids: An energy-based approach. *IEEE Journal of Emerging and Selected Topics in Industrial Electronics*, *5*(4), 1388–1395. https://doi.org/10.1109/JESTIE.2024.3425518

Guerreiro, M., Kharade, S., dos Santos, P., & Liu, S. (2022). Power electronics control with system-on-a-chip-based platforms. In *IEEE 20th International power electronics and motion control conference* (pp. 353–359). https://doi.org/10.1109/PEMC51159.2022.9962949

Hasan, M. M., Razmi, D., Babayomi, O., Davidson, I., Terzija, V., & Zhang, Z. (2025). Advanced control and protection strategies for grid-forming inverters in microgrids—a review. *International Journal of Electrical Power & Energy Systems*, *172*, 111297. https://doi.org/10.1016/j.ijepes.2025.111297

He, W., & Ortega, R. (2020). Design and implementation of adaptive energy shaping control for DC–DC converters with constant power loads. *IEEE Transactions on Industrial Informatics*, *16*(8), 5053–5064. https://doi.org/10.1109/TII.2019.2953694

Iovine, A., Rigaut, T., Damm, G., De Santis, E., & Di Benedetto, M. D. (2019). Power management for a DC MicroGrid integrating renewables and storages. *Control Engineering Practice*, *85*, 59–79. https://doi.org/10.1016/j.conengprac.2019.01.009

Isidori, A. (1995). Nonlinear control systems. London, U.K.: Springer.

Kim, S.-K., & Lee, K.-B. (2015). Robust feedback-linearizing output voltage regulator for DC/DC boost converter. *IEEE Transactions on Industrial Electronics*, *62*(11), 7127–7135. https://doi.org/10.1109/TIE.2015.2443102

Lei, Q., Arraño-Vargas, F., & Konstantinou, G. (2023). Adaptive power reserve control for photovoltaic power plants based on local inertia in low-inertia power systems. *IEEE Journal of Emerging and Selected Topics in Industrial Electronics*, *4*(3), 781–790.

Lidula, N. W. A., & Rajapakse, A. D. (2011). Microgrids research: A review of experimental microgrids and test systems. *Renewable and Sustainable Energy Reviews*, *15*(1), 186–202. https://doi.org/10.1016/j.rser.2010.09.041

Liu, X., Zhao, T., Deng, H., Wang, P., Liu, J., & Blaabjerg, F. (2023). Microgrid energy management with energy storage systems: A review. *CSEE Journal of Power and Energy Systems*, *9*(2), 483–504. https://doi.org/10.17775/CSEEJPES.2022.04290

Mayne, D. Q., Rawlings, J. B., Rao, C. V., & Scokaert, P. O. M. (2000). Constrained model predictive control: Stability and optimality. *Automatica*, *36*(6), 789–814. https://doi.org/10.1016/S0005-1098(99)00214-9

Mitali, J., Dhinakaran, S., & Mohamad, A. A. (2022). Energy storage systems: A review. *Energy Storage and Saving*, *1*(3), 166–216. https://doi.org/10.1016/j.enss.2022.07.002

Muralee Gopi, C. V. V., Alzahmi, S., Narayanaswamy, V., Vinodh, R., Issa, B., & Obaidat, I. M. (2025). Supercapacitors: A promising solution for sustainable energy storage and diverse applications. *Journal of Energy Storage*, *114*, 115729. https://doi.org/10.1016/j.est.2025.115729

Ortega, R., van der Schaft, A., Maschke, B., & Escobar, G. (2002). Interconnection and damping assignment passivity-based control of port-controlled Hamiltonian systems. *Automatica*, *38*(4), 585–596. https://doi.org/10.1016/S0005-1098(01)00278-3

Pang, S., Nahid-Mobarakeh, B., Pierfederici, S., Phattanasak, M., Huangfu, Y., Luo, G., & Gao, F. (2019). Interconnection and damping assignment passivity-based control applied to on-board DC–DC power converter system supplying constant power load. *IEEE Transactions on Industry Applications*, *55*(6), 6476–6485. https://doi.org/10.1109/TIA.2019.2938149

Rocabert, J., Capó-Misut, R., Muñoz-Aguilar, R. S., Candela, J. I., & Rodriguez, P. (2019). Control of energy storage system integrating electrochemical batteries and supercapacitors for grid-connected applications. *IEEE Transactions on Industry Applications*, *55*(2), 1853–1862. https://doi.org/10.1109/TIA.2018.2873534

Rosso, R., Wang, X., Liserre, M., Lu, X., & Engelken, S. (2021). Grid-forming converters: Control approaches, grid-synchronization, and future trends—a review. *IEEE Open Journal of Industry Applications*, *2*, 93–109. https://doi.org/10.1109/OJIA.2021.3074028

Shahrouei, Z., Rahmati, M., Gavagsaz-Ghoachani, R., Phattanasak, M., Martin, J.-P., & Pierfederici, S. (2023). Robust flatness-based control with nonlinear observer for boost converters. *IEEE Transactions on Transportation Electrification*, *9*(1), 142–155. https://doi.org/10.1109/TTE.2022.3192217

Sharma, J., Sundarabalan, C. K., & Balasundar, C. (2025). Advanced energy management strategy for enhancing battery lifespan in solar PV-powered EV charging stations with hybrid energy storage systems. *Renewable Energy*, *251*, 123443. https://doi.org/10.1016/j.renene.2025.123443

Srinivasan, M., & Kwasinski, A. (2020). Control analysis of parallel DC-DC converters in a DC microgrid with constant power loads. *International Journal of Electrical Power & Energy Systems*, *122*, 106207. https://doi.org/10.1016/j.ijepes.2020.106207

Wang, L. (2009). Model predictive control system design and implementation using MATLAB. London, U.K.: Springer.

Xu, L., Ma, R., Xie, R., Zhuo, S., Huangfu, Y., & Gao, F. (2023). Offset-free model predictive control of fuel cell DC–DC boost converter with low-complexity and high-robustness. *IEEE Transactions on Industrial Electronics*, *70*(6), 5784–5796. https://doi.org/10.1109/TIE.2022.3198249

Zhang, C., Li, M., Zhou, L., Cui, C., & Xu, L. (2023). A variable self-tuning horizon mechanism for generalized dynamic predictive control on DC/DC boost converters feeding CPLs. *IEEE Journal of Emerging and Selected Topics in Power Electronics*, *11*(2), 1650–1660. https://doi.org/10.1109/JESTPE.2022.3225264

Zhang, X., Yi, H., Wen, Y., Li, Q., Wang, Z., Luo, Y., & Zhuo, F. (2024). Decentralized control of multiple supercapacitors for hybrid energy storage converter in off-grid mode under power fluctuations and short-time high power. *IEEE Transactions on Industry Applications*, *60*(5), 7225–7239. https://doi.org/10.1109/TIA.2024.3406669